Transition to chaos in a laser system with delayed feedback

J. Simonet and E. Brun

Physik Institut der Universität Zürich, CH-8057 Zürich, Switzerland

R. Badii

Paul Scherrer Institute, CH-5232 Villigen, Switzerland

The transition from quasiperiodicity to chaos in an NMR laser with delayed feedback is investigated both experimentally and numerically. We concentrate on the low-delay-time region where stable tori arise either from a sequence of two Hopf bifurcations or from an "interaction" between mutually transversal unstable limit cycles. Transitions to chaos via intermittency and crises have been observed, as well as the "fractalization" of tori.

PACS number(s): 05.45.+b, 76.60.−k

I. INTRODUCTION

The study of low-dimensional chaos in dissipative systems [1,2] has provided quite a complete understanding both of the ways in which stable motion turns into aperiodic, unpredictable behavior ("routes to chaos" [3–5]) and of the structure of the chaotic attractors arising with these mechanisms [6,7]. In addition to a global characterization of chaos through fractal dimensions [8–11], entropies [12–14], and Lyapunov exponents [15,16,1], a more detailed analysis based on the location of unstable periodic orbits [17–19] and on the construction of the symbolic dynamics [20] has been successfully carried out in numerical simulations and experimental systems [21–23].

The study of these aspects of nonlinear systems (transitions to chaos, global and local characteristics of the attractors, and periodic-orbit structure) is much more difficult whenever the dimension of the invariant set is larger than just 3 or 4. This intermediate class of systems has received relatively little attention, although the investigation of symbolic dynamics and thermodynamic properties [24–27,7,28,29] of the invariant measures is expected to reveal new interesting phenomena. Most of the recent efforts have been directed toward spatially extended systems, which exhibit a large number of qualitatively different kinds of behavior. In particular, the definition of spatiotemporal chaos itself is still controversial [30–33].

In the attempt to simplify the analysis of fully spatiotemporal phenomena and take advantage of the experience made with low-dimensional systems, a class of model systems have been further introduced, namely, the so-called coupled map lattices [34]. In those systems both time and space are discretized so that connections with real, continuous systems are not immediate. Dynamical behavior unfolding in medium- and high-dimensional phase space can, however, be generated by experimentally realizable continuous systems as well, without involving any spatial dependence. The best known example is provided by delay differential equations of the form

$$\dot{\mathbf{x}} = \mathbf{F}(\mathbf{x}(t), \mathbf{x}(t - \tau)) , \tag{1}$$

where $\mathbf{F}$: $\mathbb{R}^d \rightarrow \mathbb{R}^d$ is a nonlinear function, $\mathbf{x} \in \mathbb{R}^d$ is the state variable, and τ is the delay time. Models of this type naturally arise in various fields, such as optics [35,36], biology, and physiology [37]. Since the future evolution depends on a continuous range of $\mathbf{x}$ values [all those in the time interval $(-\tau, 0)$], the dimension of phase space is infinite. It has been proved, however, that the attractors are finite dimensional, under rather general assumptions [38] (see [39] for a related conjecture). The dimension has been shown to increase proportionally to τ for $\tau \rightarrow \infty$, while the values of the Lyapunov exponents decrease as $1/\tau$, so that the metric entropy (related to the integral of the positive part of the Lyapunov spectrum) converges to a finite value [40]. These results have been confirmed in [41] for a continuous system and in [42] for delayed maps.

In the present work, we investigate bifurcation structure and transitions to chaos in a nuclear-magnetic-resonance (NMR) laser [23] for which a mathematical model is available in the form of a low-dimensional set of ordinary differential equations [43,21]. Previous investigations focused on low-dimensional chaotic behavior, obtained by periodically modulating some system parameter. The extraction of the unstable periodic orbits and the analysis of the symbolic dynamics obtained from them have revealed that a set of modified Bloch-type equations proposed in [43] reproduces the experimental observations with great precision. Hence the NMR laser represents an ideal system to study the effect of a delayed feedback on a nonlinear device, both experimentally and theoretically (see, for example, [44]). In particular, we present a detailed linear stability analysis for the basic Hopf bifurcation and give evidence for intermittency, crises, and torus breakup via a "fractalization" process. Attractors with dimension larger than 3 have been observed also in the short-delay region.

II. EXPERIMENTAL SETUP

A laser consists of three main parts: the radiating particles, the radiation field produced by them in a resonant

structure (cavity), and a mechanism to achieve population inversion. For the NMR laser, the active particles are the ^{27}Al nuclear spins $(I=\frac{5}{2})$ in ruby crystal Al_2O_3:Cr^{+3} subjected to a static magnetic field B_0 of the order of 1.2 T. The radiation field corresponds to the magnetization M_v transverse to the field B_0 produced by the nuclear spins. The ruby crystal is placed within a coil that is part of an inductance-capacitance (LC) circuit, providing feedback for the radiation field. This LC circuit represents the cavity of the laser. Spin inversion is obtained by means of dynamic nuclear polarization [45]. By shining microwaves $(v \approx 30$ GHz) at Cr^{+3}, electronic transitions are caused that pump the nuclear spins to the lasing state. The induced voltage in the LC circuit is tapped at the capacitive voltage splitter (C_1, C_2) (Fig. 1), demodulated, and amplified, thus providing the laser output $v(t)$. As will be shown below, the NMR laser can be described by a set of only two differential equations under the experimental conditions chosen in our investigation. To make chaotic behavior possible an additional degree of freedom is necessary. Experimentally, this is realized by varying a system parameter in time. In our case, the resistance of the LC circuit is varied, thus changing its quality factor Q. This is done with the help of a p-i-n diode (see Fig. 1), the resistance of which depends on the voltage $v_{p\text{-}i\text{-}n}$ applied to it. The influence of the p-i-n-diode on the quality factor is expressed by

$$Q(t) = Q_0 - pv_{p\text{-}i\text{-}n}(t) \ . \tag{2}$$

where the sensitivity p has been determined experimentally and Q_0 is the unperturbed quality factor.

The p-i-n diode is driven by the output signal of the laser, delayed as follows. The laser signal is digitized, stored in a memory buffer, and fed back into the electronic circuitry after the chosen delay time τ. As a result,

$$v_{p\text{-}i\text{-}n}(t) = v(t-\tau) \ . \tag{3}$$

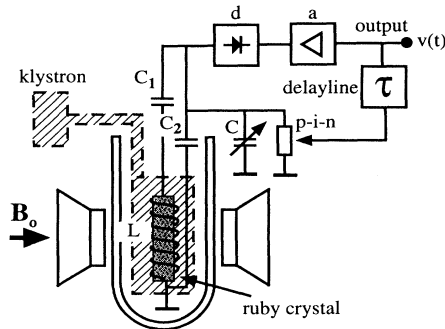The application of Faraday's law for the voltage induced

FIG. 1. Schematic representation of the experimental setup for the ruby NMR laser with delayed feedback. The gain medium consists of the nuclear spins of the ^{27}Al nuclei within a ruby crystal that is subjected to a static field B_0. Population inversion is obtained by dynamic nuclear polarization with microwaves supplied by a klystron. The resonator is composed of a coil L, a capacitive voltage splitter (C_1, C_2) and a tuning capacitor C, and a variable resistor (p-i-n diode). The laser output is fed back to the p-i-n diode after a delay time τ.

in the coil and of Kirchhoff's laws for the LC circuit yields

$$v(t) = \delta\mu_0\eta AN\omega_c Q(t)|M_v(t)| \ , \tag{4}$$

where δ is an amplification factor, μ_0 the permeability of free space, η the filling factor, A the cross section of the coil, N the number of its windings, and ω_c the laser frequency v_c times 2π (see Table I).

To simplify the notation we define $q(t) = Q(t)/Q_0$ and $\epsilon = p\delta\mu_0\eta AN\omega_c$, which leads to the equation

$$q(t) = 1 - \epsilon q(t-\tau)|M_v(t-\tau)| \tag{5}$$

for $q(t)$. Hence the feedback mechanism not only renders the dynamics dependent on past values of the variables but also induces a "recursive" structure in $Q(t)$.

III. LINEAR STABILITY ANALYSIS

The single-mode dynamics of the NMR laser in a suitable rotating frame is accurately reproduced by the extended Bloch model (EBM) [43,23]

$$\dot{B}_u = -\kappa B_u - \chi M_v \ ,$$

$$\dot{M}_v = -\gamma_\perp M_v(1 + \alpha|M_v|/3) + 9gM_z B_u \ , \tag{6}$$

$$\dot{M}_z = -\gamma_\parallel(M_z - M_e) - gM_v B_u \ ,$$

where B_u is the transverse component of the radiation magnetic field and M_v and M_z are, respectively, the transverse and longitudinal components of the nuclear magnetization. The parameters κ, $\gamma_\perp$, and $\gamma_\parallel$ are phenomenological damping constants, g is the gyromagnetic ratio of the ^{27}Al spins, and α is a coefficient that accounts for nonlinear effects in the relaxation mechanism for the transverse magnetization. The decay rate κ of the field B_u is given by

$$\kappa = \frac{\omega}{2Q(t)} \ , \tag{7}$$

where $\omega_c = 2\pi v_c$ and v_c is the laser frequency. The values of the various system parameters are reported in Table I.

The laser equations can be rewritten in a more con-

TABLE I. Experimentally determined NMR laser parameters for standard running conditions.

NMR laser parameters	Value	Unit
gyromagnetic ratio g	6.97×10^7	1/s T
quality factor Q_0	310	
static NMR field B_0	1.109	T
laser frequency v_c	12.3×10^6	Hz
pump magnetization M_e	-0.75	A/m
longitudinal pump rate $\gamma_\parallel$	4.76	1/s
transverse decay rate $\gamma_\perp$	2.38×10^4	1/s
EBM dephasing coefficient α	0.607	m/A
filling factor η	0.42	
coupling constant χ	10.19	T m/A s
number of windings N	30	
cross section of the NMR coil A	47.746×10^{-6}	m^2

venient form by introducing the adimensional variables

$$x = \frac{3g}{\gamma_\perp}B_u, \quad y = -2\beta M_v, \quad z = 6\beta(M_z - M_e), \quad (8)$$

with $\beta = 3g\chi Q_0/(\omega_c\gamma_\perp)$. By taking the derivatives with respect to the adimensional time $t' = t\gamma_\perp$, the EBM equations read

$$\dot{x} = -\sigma'[x/q'(t') - y],$$
$$\dot{y} = -y(1 + ay) + rx - xz, \quad (9)$$
$$\dot{z} = -bz + xy,$$

where

$$q'(t') = 1 - \epsilon'q'(t' - \tau')y(t' - \tau') \quad (10)$$

is the reduced quality factor q, expressed as a function of t', and $\epsilon' = \epsilon/2\beta$. The parameters in Eq. (9) have the expressions

$$\sigma' = \frac{\omega_c}{2Q_0\gamma_\perp}, \quad r = 6\beta|M_e|, \quad a = \alpha/6\beta, \quad b = \frac{\gamma_\parallel}{\gamma_\perp}. \quad (11)$$

In order to simplify the analysis, it is useful to normalize the variables x, y, and z to the fixed-point values

$$x = y = x_\pm = \pm\sqrt{b(r-1)}, \quad z = z_0 = r - 1 \quad (12)$$

of the Lorenz system ($a = \epsilon' = 0$, $r > 1$) according to

$$(X, Y, Z) = [x/x_+, y/x_+, (z - z_0)/x_+] \quad (13)$$

and to introduce a time $t = x_+ t'$ [not to be confused with the physical time appearing in Eqs. (2), (4), and (5)], so that

$$\dot{X} = -\sigma[X/q(t) - Y],$$
$$\dot{Y} = -Y(A + aY) + X(A - Z), \quad (14)$$
$$\dot{Z} = -BZ - 1 + XY,$$

where

$$q(t) = 1 - \epsilon q(t - \tau)Y(t - \tau), \quad (15)$$

with $\epsilon = \epsilon'x_+ \in [0, 3 \times 10^{-2}]$, $\sigma = \sigma'/x_+ \approx 494$, $A = x_+^{-1} \approx 101.32$, $a \approx 0.301$, and $B = b/x_+ \approx 2.0265 \times 10^{-2}$. Since the parameter σ is much larger than any other damping constant (1 for Y and B for Z), the X variable quickly relaxes to its regime value $Yq(t)$ and can be adiabatically eliminated. In the resulting system

$$\dot{Y} = -Y[A + aY + q(t)(Z - A)],$$
$$\dot{Z} = -BZ - 1 + q(t)Y^2, \quad (16)$$

it is readily noticed that the variable Y never changes sign since its derivative vanishes with Y itself [for this reason, no absolute value has been taken for the y variable already in Eq. (9)]. The most natural variable to use is hence $S = \ln Y$, which finally yields the desired form

$$\dot{S} = -A - ae^S + q(t)(A - Z),$$
$$\dot{Z} = -BZ - 1 + q(t)e^{2S}. \quad (17)$$

When the control parameter ϵ is zero, the system admits a stable fixed point, which, upon increase of ϵ, gives rise to a limit cycle at a value $\epsilon_H = \epsilon_H(\tau)$, where a Hopf bifurcation occurs. In order to study this phenomenon analytically, we consider not only ϵ but also a and B as small parameters, while $A \gg 1$. To order 0 (i.e., $a = \epsilon = 0$), the system can be rewritten in the form of a damped Toda oscillator

$$\dot{S} = P, \quad \dot{P} = -BP + 1 - e^{2S}, \quad (18)$$

where $P = -Z$ and the potential is $V(S) = e^{2S}/2 - S$. The eigenfrequency $\omega_0 = \sqrt{2}$ at the fixed point $(S_0, Z_0) = (0, 0)$, for $B = 0$, corresponds to a physical eigenperiod of 18.9 ms, the scaled one being $T_0 = 2\pi/\omega_0 \approx 4.44$. The order-1 coordinates (S_1, Z_1) of the fixed point are obtained by setting

$$q = q_1 = 1 - \epsilon q_1 e^{S_1}$$

and by retaining terms with magnitude up to approximately 10^{-3} (e.g., a^2B or $\epsilon^2 A$):

$$S_1 \approx -\epsilon\frac{AB - 1}{2} - \frac{aB}{2},$$
$$Z_1 \approx -a + a^2\frac{B}{2} - A\epsilon - \frac{a\epsilon}{2} + a\epsilon AB + \epsilon^2 A\frac{AB - 1}{2}. \quad (19)$$

Substituting

$$S = S_1 + se^{\lambda t}, \quad Z = Z_1 + \zeta e^{\lambda t}, \quad q = q_1 + ce^{\lambda t}$$

into Eq. (17) and carrying out all necessary simplifications to the appropriate order in ϵ, a, A, and B, one arrives at the equation

$$\lambda + B \approx \frac{-2q_1^2 e^{2S_1}}{A\epsilon q_1 e^{S_1}e^{-\lambda\tau} + ae^{S_1} + \lambda}, \quad (20)$$

which yields λ implicitly in terms of the two control parameters ϵ and τ. It is readily verified that the instability threshold $\lambda = 0$ cannot be attained with real λ. Hence the bifurcation of the fixed point (S_1, Z_1) is of the Hopf type, that is, $\lambda = \lambda' + i\lambda''$ is a complex eigenvalue of the system. When its expression is substituted into Eq. (20), one obtains two coupled equations that have to be solved for a function $\epsilon(\tau)$ by imposing the marginality condition $\lambda' = 0$. As a result, one obtains the bifurcation curve of the fixed point in parameter space (τ, ϵ) and the frequency $\lambda''(\tau) = \omega(\tau)$ of the limit cycle arising from the bifurcation. Owing to the presence of the trigonometric terms $\sin(\omega\tau)$ and $\cos(\omega\tau)$ in the stability equations, the solutions $\epsilon(\tau)$ and $\omega(\tau)$ are families of curves, as can be seen from Fig. 2, in which we report the results of a numerical evaluation of the eigenvalue equation (20). The actual bifurcation curve $\epsilon_H(\tau)$ is the continuous one that joins the lowermost intersection points of adjacent members of such families, since it marks the instability of the fixed point as soon as it is reached upon increase of ϵ. The open circles in the figure have been obtained with a direct integration of the differential equations (17), while the full triangles correspond to experimental values. The corresponding symbols in the lower figure show that a frequen-

cy jump occurs at $\tau = \tau_k = kT_0$ when the new solution (limit cycle) appears just beyond the next branch of the bifurcation family. Hysteresis may occur, but it has not been resolved experimentally. For related phenomena see [46].

IV. FORMATION AND BREAKUP OF TORI

The phenomenology of the delayed NMR laser can be discussed with reference to Fig. 3, where the delay-amplitude parameter space (τ, ϵ) is represented in the short-delay domain. In addition to the Hopf-bifurcation curves discussed above, we display the main regions of stable periodic behavior with a gray coding. Figure 3(a) has been obtained with a numerical integration of Eq. (17) whereas 3(b) shows the corresponding experimental data (experimental units are used everywhere); an enlargement of the framed area in 3(a) is displayed in 3(c). The white region in Figs. 3(a) and 3(b) indicates the stable fixed point and the light gray one the Hopf limit cycle: notice the agreement between the numerical integration and the linear stability analysis. The darker areas denote higher-order periodic solutions and aperiodic motion. The upper left part of each "tongue" (coded in medium-dark gray) corresponds to a period-2 orbit. On the right of the tongues, for ϵ approximately in the range (0.5,0.7), one observes periodic orbits of increasing length: period two in the first tongue [medium gray in the enlargement (c)], period three in the second (black), and so on. The
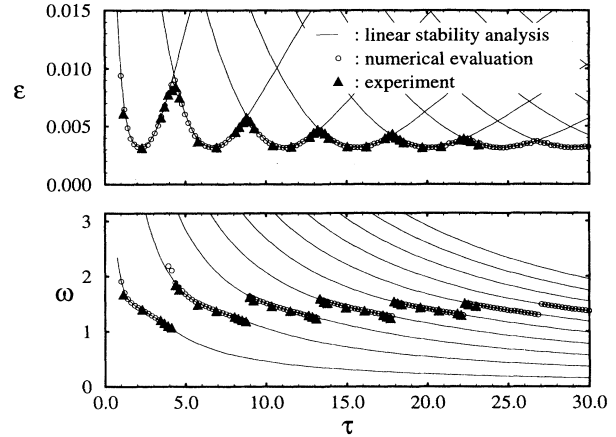

FIG. 2. Results of the linear stability analysis: (a) amplitude ϵ of the feedback signal as a function of the delay time τ at which the fixed point undergoes a Hopf bifurcation; (b) frequency ω of the limit cycle arising from the bifurcation, versus τ. The open circles correspond to the numerical integration of the EBM and the triangles to the experiment.

extension of all these "flanking" regions reduces with increasing order of the tongue. In the interior of the tongues one observes quasiperiodic (two-frequency tori or 2-tori) and chaotic motions, which become "generic" for large delay times [no chaos occurs, however, within the enlargement of Fig. 3(c)]. The fractal dimension, estimat-
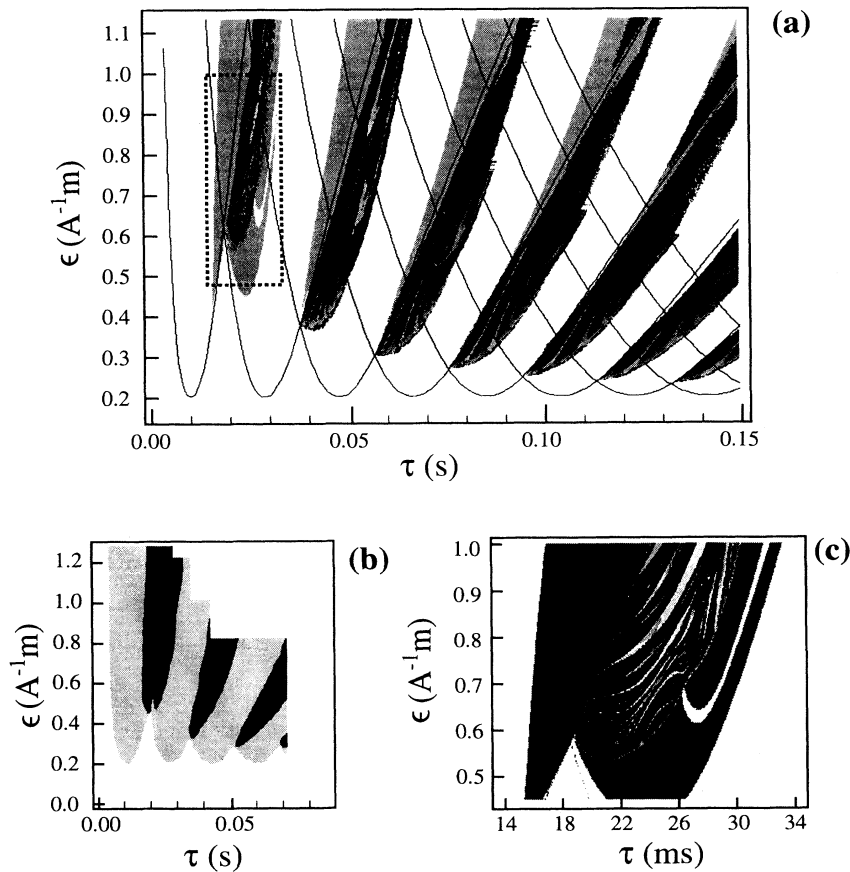

(a)

(b)

(c)

FIG. 3. Overview of the phenomenology in parameter space (τ, ϵ). The gray coding corresponds to the number of different maxima detected in a fixed finite portion of the signal. The white region corresponds to the stable fixed points, light gray to a stable limit cycle, and darker regions to signals with increasing number of different maxima (including chaotic behavior): (a) model, (b) experiment, and (c) enlargement of the boxed area in (a).

ed with the nearest-neighbor method [10,47], never exceeds 4 for short delay but can be larger than 3.

As a further illustration of the type of attractors exhibited by the system and of the accuracy of the EBM, we show in Fig. 4 two stable limit cycles, one torus, and a chaotic attractor, reconstructed from experimental (left) and numerical (right) time series $\{v(n)\}$, where $v(n)=v(n\Delta t)$ and Δt is a sampling time of the order of $\frac{1}{5}$ of the length of the period-1 cycle. They are observed when moving horizontally across the third tongue of Fig.

3 from left to right at $\epsilon=0.5972$.

Tori do not appear only well inside the tongues but also in the vicinity of the cusps of the Hopf bifurcation curve. The formation of one such torus is illustrated in Fig. 5 for a delay $\tau\approx13.34$ (0.0565 s), that is, slightly on the right of the third cusp from the left in Fig. 3. For low values of the feedback amplitude (e.g., $\epsilon=0.00468$), one observes the limit cycle C_1, which then bifurcates to a 2-torus (T_1), displayed here for $\epsilon=0.004685$. By further increasing ϵ to 0.00469, one obtains the torus T_0 shown on the right in the figure. In turn, T_0 undergoes an "inverse" bifurcation to the torus T_2, displayed for $\epsilon=0.0046945$. A further increase of ϵ to 0.004695 finally yields the limit cycle C_2. It must be noticed that C_1 and T_1 are transversal to C_2 and T_2. In fact, when the minor axis of T_1 gets sufficiently large, the trajectory starts experiencing the motion in the "direction" of C_2 and T_0 appears. In the competition between the two directions, the second one survives for larger ϵ values. The two extreme cycles of this process belong to the light-gray regions to the right (C_1) and to the left (C_2) of the above-mentioned cusp. The two frequencies of these cycles and of torus T_0 are those found with the linear stability analysis: they belong to the two adjacent (τ,ω) curves (Fig. 2, bottom) at which the third jump occurs. The two frequencies of tori T_1 and T_2 are only slightly different. These solutions come arbitrarily close to each other at the cusp. In the large-τ limit, the frequency jumps become smaller and smaller: both the bifurcation frequency and the bifurcation line tend to a constant. Qualitatively different types of attractors may then occur as shown in Ref. [48], where the appearance of "defects" has been documented in a spatiotemporal representation for delay systems. We have observed attractors with relatively large dimension (above 4), which, however, are not studied here for reasons of brevity.

In order to discuss the nature of the transition into chaos, let us first consider the bifurcation diagram displayed in Fig. 6, where we report the local maxima of the time series, recorded at $\epsilon=0.009$ for τ in the range (15.3,19). Notice the bifurcation of a period 2 to a torus at $\tau\approx16.4$. Windows of periodic motion ("locked" states) occur within the initial quasiperiodic regime,

FIG. 4. Two-dimensional projections of the laser output $v(n)=v(n\Delta t)$, suitably rescaled and embedded using a sampling time Δt of the order of $\frac{1}{5}$ of the length of the period-1 cycle. The orbits are observed at a fixed value of the feedback amplitude $\epsilon=0.5972$ and at four values of the delay time τ (from top to bottom): 0.074, 0.077, 0.079, and 0.083 s. Left column, experiment; right column, model.
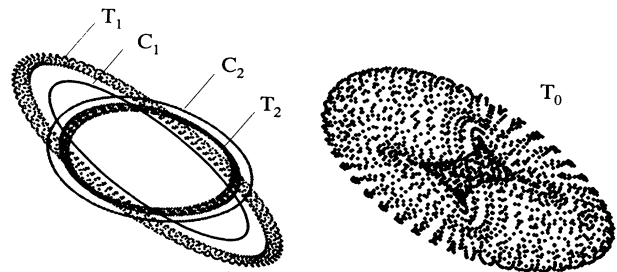

FIG. 5. Three-dimensional representations of stable regular attractors at $\tau=13.34$. Mutually transversal (limit cycle, torus) pairs, observed below (C_1,T_1) and above (C_2,T_2) the torus T_0, are displayed on the left. They occur at the parameter values $\epsilon=0.00468$ (C_1), $\epsilon=0.004685$ (T_1), $\epsilon=0.00469$ (T_0), $\epsilon=0.0046945$ (T_2), and $\epsilon=0.004695$ (C_2).
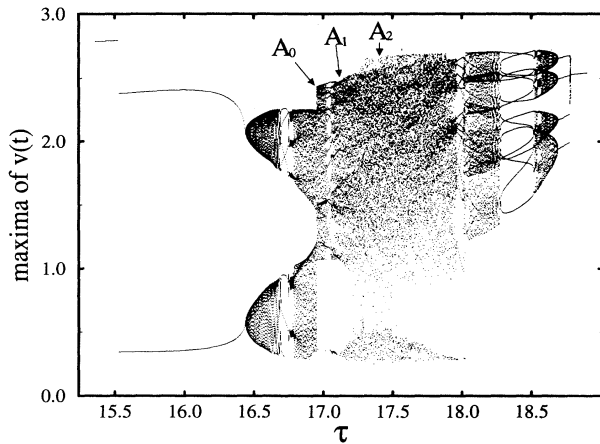
FIG. 6. Bifurcation diagram of the NMR laser at $\varepsilon = 0.009$, computed from the model. The bifurcation parameter is the adimensional delay time τ. Notice the tori arising from Hopf bifurcations at both extrema of the diagram.

FIG. 8. Intersection of the torus existing at the left of point A_0 in Fig. 6 with the Poincaré section (bean-shaped closed curve in the middle). The same arbitrary scale has been used for the two axes (which correspond to linear combinations of the coordinates in embedding space). Upon little increase of the delay time τ, this torus becomes unstable and a new one (large closed curve) appears after a transient, also displayed in the figure (large dots). To guide the eye, five outgoing paths have been drawn explicitly with arrows.

which apparently ceases because of a sudden transition at $\tau \approx 16.938$ (point A_0 in the figure). In order to illustrate this phenomenon, we took a Poincaré section Σ in embedding space, as shown in Fig. 7 for the torus at $\tau = 16.6$. The attractor existing just to the left of A_0 yields, in Σ, the closed bean-shaped curve appearing in the central part of Fig. 8. Upon a tiny increase of τ, this solution becomes unstable and the system lands, after a transient also displayed in Fig. 8, to a new stable torus that intersects Σ at the points forming the outer closed curve in Fig. 8. Five sets of transient points have been put in evidence by joining their members with continuous lines to show the direction of the trajectories: a point in one of these sets is mapped to one of another set and so on until its image returns to the original set, at a larger distance from the inner torus. The direction of the spiraling motion is further indicated by arrows. Hence this
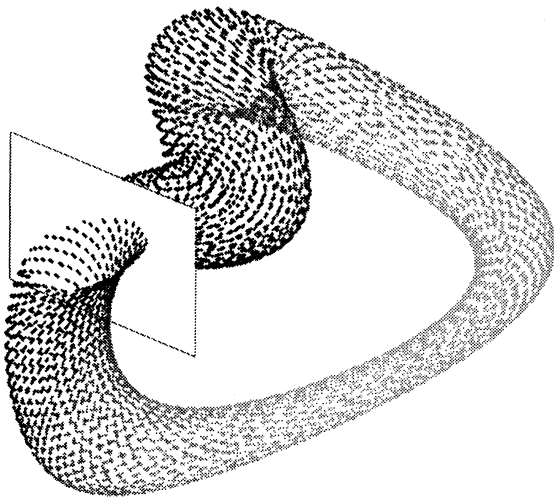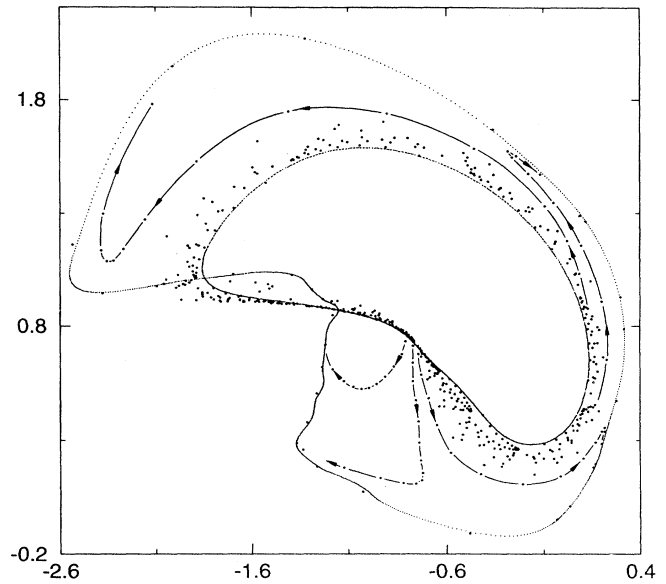
transition is an intermittent one. For completeness, we show the circle maps (Fig. 9) corresponding to the two tori [(a) for the inner one and (b) for the outer one] obtained by choosing a point on Σ [at $(-0.25, 1.2)$ in an arbitrary logarithmic scale for the variable S] and plotting pairs of consecutively occurring angles, calculated with respect to a fixed reference direction. Although the resulting curves are close to the diagonal, no "angular" intermittency occurs. The instability is associated with the radial direction. The torus generated at A_0 changes its shape upon increase of the delay time, collapses to a period-17 stable cycle, reappears, and finally takes the shape displayed in Fig. 10(a). At this point, just to the left of A_1 in Fig. 6 ($\tau = 17.1037$), the torus lies close to the stable manifold of the period 17, which, in the mean-
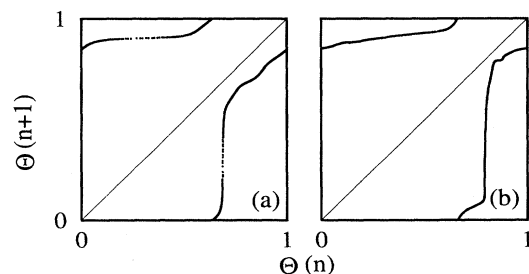

FIG. 7. Three-dimensional representation of the torus appearing at $\varepsilon = 0.009$ and $\tau = 16.6$ (see Fig. 6). The plane yielding the Poincaré section is shown.

FIG. 9. Circle maps for the tori in Fig. 8: (a) the smaller torus and (b) the larger torus. The angle $\Theta_n (\mathrm{mod} 2\pi)$ has been computed using the same origin and reference direction for the two pictures.
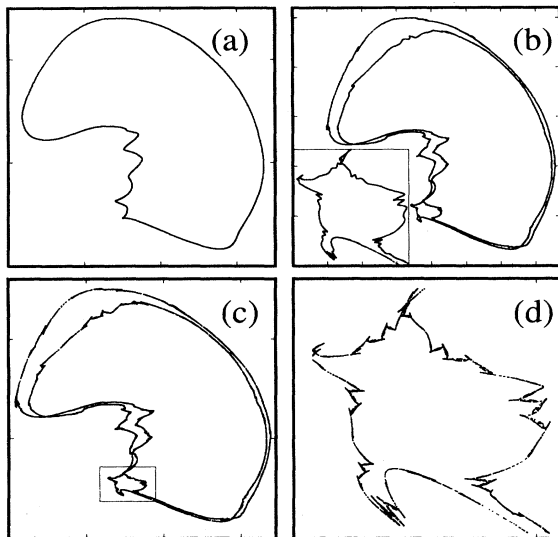
FIG. 10. Evolution of the larger torus of Fig. 8 upon increase of the delay time τ: (a) $\tau = 17.1037$, (b) $\tau = 17.1274$, and (c) and (d) $\tau = 17.1345$ (see point A_1 in Fig. 6). The coordinates are chosen as in Fig. 8. In (b), the torus is doubled and presents a large number of smooth folds, some of which can be seen in the enlargement. In (c), the torus has collided with the stable manifold of an unstable period-17 orbit and turned into a strange attractor. The enlargement in (d) shows a large but finite number of sharp bends and reveals a finite width of the transversal sections of the attractor.

time, turned unstable. After a doubling, the torus approaches further that manifold [see Fig. 10(b), showing the torus at $\tau = 17.1274$]. The enlargement of part of the attractor helps verify that still a smooth curve is observed. Finally, at $\tau = 17.1345$, the collision of the torus with the stable manifold of the period 17 has taken place, with a consequent repulsion along the unstable manifold and the creation of homoclinic intersections. The resulting strange attractor and a magnified portion of it are displayed, respectively, in Figs. 10(c) and 10(d). Notice that the attractor indeed has a transversal structure with a finite diameter. The curve at the transition point, although reminiscent of a fractal, does not present truly sharp bends at all scales. It is natural to conjecture, however, that fractalization of tori at the chaotic transition becomes generic for large delay times.

Finally, we briefly illustrate the structure of the strange attractor existing at point A_2 in Fig. 6. Its Poincaré section, a projection of which is displayed in Fig. 11, clearly shows that its dimension is larger than 3: in fact, the picture reveals a complicated topology with folds and holes typical of an object embedded in an at least three-dimensional space. Indeed, a dimension estimate, carried out with the nearest-neighbor (NN) method [10,47], yields the result $D(0) \approx 3.3$ for the information dimension. The results of this analysis are shown in Fig. 12. In Fig. 12(a) we report the logarithmic average of the distance δ to the kth NN as a function of the number of points n on the attractor (logarithms to base 1.18 have been used), for embedding dimension E between 1 and 15

and NN order $k = 40$. In Fig. 12(b) the dimension estimates are plotted versus the embedding dimension for $k = 10$, 20, 30, and 40: these values have been obtained from the slopes of the curves in Fig. 12(a), computed in the asymptotic regime (log $n \geq 60$), except for $E = 1$, where $40 \leq \log n \leq 50$. Notice the good convergence of the data with increasing embedding dimension.

The point at which the information dimension $D(0)$ becomes larger than 3 has not been precisely located yet. As may be observed in Fig. 6, a sharp transition takes place at $\tau \approx 17.2$, with structural changes in the attractor. An analysis of this transition, performed with the help of the Lyapunov spectrum, is therefore deferred to future investigations.

V. CONCLUSIONS

We have studied an experimental system with delayed feedback, applied at parameter values that do permit chaotic motion. The effect of the increase of phase space was to yield limit cycles of all periods, two-frequency tori, and chaos. The accuracy of the extended Bloch
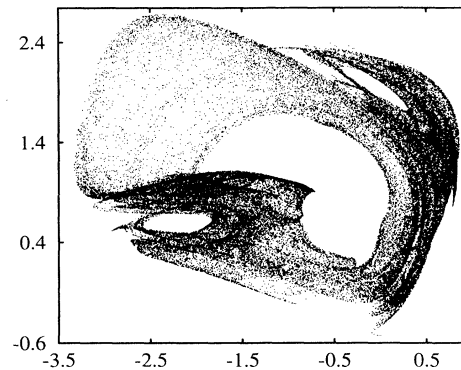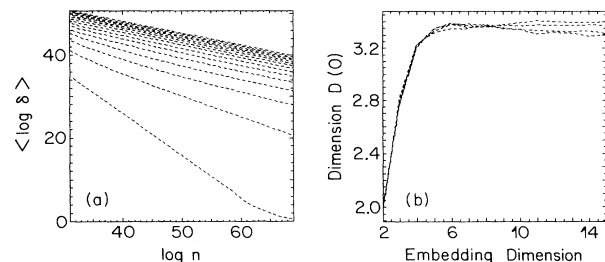

FIG. 11. Poincaré section of the strange attractor existing at point A_2 in Fig. 6. The coordinates are chosen as in Fig. 8. Notice the higher-dimensional topology of this set, clearly visible also in this two-dimensional projection.

FIG. 12. Results of the dimension analysis for the attractor of Fig. 11. In (a), we report the logarithmic average of the distance δ between a point and its 40th nearest neighbor (NN) versus the logarithm of the number n of points on the attractor for embedding dimension E between 1 (bottom) and 15 (top). Logarithms are to base 1.18. In (b), the estimated information dimension $D(0)$ is plotted as a function of the embedding dimension for NN order $k = 10,20,30,40$ (from the bottom). The asymptotic value is $D(0) = 3.275 \pm 0.025$.

laser model has been confirmed also in these operating conditions. Moreover, the model has allowed us to follow very closely a few interesting transitions, including the breakup of a torus with a complicated fold structure, with a precision that cannot be achieved experimentally. Finally, we presented a strange attractor with dimension higher than 3 and an interesting topology.

The phenomenology observed in this paper suggests deepening the study by considering the periodic-orbit structure of the system and constructing the symbolic dynamics of the higher-dimensional attractors that are gen-erated already for relatively short delay times. Moreover, the relationship between the Lyapunov exponents and the passage of the dimension through the value 3 deserves particular attention since universal features might appear. We plan to address these issues in a future paper.

ACKNOWLEDGMENTS

[1] J.-P. Eckmann and D. Ruelle, Rev. Mod. Phys. **57**, 617 (1985).

[2] J. Guckenheimer and P. Holmes, *Nonlinear Oscillations, Dynamical Systems, and Bifurcations of Vector Fields,* Applied Mathematical Sciences Vol. 42, 2nd ed. (Springer, New York, 1986).

[3] P. Cvitanović, *Universality in Chaos* (Hilger, Bristol, 1984).

[4] H. G. Schuster, *Deterministic Chaos* (VCH, Weinheim, 1988).

[5] A. J. Lichtenberg and M. A. Lieberman, *Regular and Chaotic Dynamics,* Applied Mathematical Sciences Vol. 38, 2nd ed. (Springer, New York, 1992).

[6] E. Ott, *Chaos in Dynamical Systems* (Cambridge University Press, New York, 1993).

[7] P. Grassberger, R. Badii, and A. Politi, J. Stat. Phys. **51**, 135 (1988).

[8] P. Grassberger, T. Schreiber, and C. Schaffrath, Int. J. Bif. Chaos **1**, 521 (1991).

[9] P. Grassberger and I. Procaccia, Phys. Rev. Lett. **50**, 346 (1983).

[10] R. Badii and A. Politi, J. Stat. Phys. **40**, 725 (1984).

[11] G. Mayer-Kress, *Dimensions and Entropies in Chaotic Systems* (Springer, Berlin, 1986).

[12] P. Billingsley, *Ergodic Theory and Information* (Wiley, New York, 1965).

[13] I. P. Cornfeld, S. V. Fomin, and Ya. G. Sinai, *Ergodic Theory* (Springer, New York, 1982).

[14] P. Walters, *An Introduction to Ergodic Theory,* 2nd ed. (Springer, New York, 1985).

[15] V. I. Oseledec, Moscow Math. Soc. **19**, 197 (1968).

[16] Ya. B. Pesin, Russ. Math. Surv. **32**, 55 (1977).

[17] D. Auerbach, P. Cvitanović, J. P. Eckmann, G. Gunaratne, and I. Procaccia, Phys. Rev. Lett. **58**, 2387 (1987).

[18] P. Cvitanović, Phys. Rev. Lett. **61**, 2729 (1988).

[19] Chaos **2** (1) (1992), special issue on periodic orbits, edited by P. Cvitanović.

[20] V. M. Alekseev and M. V. Yakobson, Phys. Rep. **75**, 290 (1981).

[21] L. Flepp, R. Holzner, E. Brun, M. Finardi, and R. Badii, Phys. Rev. Lett. **67**, 2244 (1991).

[22] M. Finardi, L. Flepp, J. Parisi, R. Holzner, R. Badii, and E. Brun, Phys. Rev. Lett. **68**, 2989 (1992).

[23] R. Badii, E. Brun, M. Finardi, L. Flepp, R. Holzner, J. Parsi, C. Reyl, and J. Simonet, Rev. Mod. Phys. **66**, 1389 (1994).

[24] R. Bowen, *Equilibrium States and the Ergodic Theory of Anosov Diffeomorphisms,* Lecture Notes in Mathematics Vol. 470 (Springer, New York, 1975).

[25] D. Ruelle, *Thermodynamic Formalism,* Encyclopedia of Mathematics and its Applications (Addison-Wesley, Reading, MA, 1978), Vol. 5.

[26] Ya. C. Sinai, Russ. Math. Surv. **27**, 21 (1972).

[27] T. C. Halsey, M. H. Jensen, L. P. Kadanoff, I. Procaccia, and B. Shraiman, Phys. Rev. A **33**, 1141 (1986).

[28] R. Badii, Riv. Nuovo Cim. **12**, 1 (1989).

[29] C. Beck and F. Schlögl, *Thermodynamics of Chaotic Systems* (Cambridge University Press, Cambridge, 1993).

[30] M. C. Cross and P. C. Hohenberg, Rev. Mod. Phys. **65**, 851 (1993).

[31] P. Manneville, *Dissipative Structures and Weak Turbulence* (Academic, Boston, 1990).

[32] J. P. Gollub, Physica D **51**, 501 (1991).

[33] J. P. Crutchfield and K. Kaneko, in *Directions in Chaos,* edited by B.-L. Hao (World Scientific, Singapore, 1987), p. 272.

[34] K. Kaneko, Prog. Theor. Phys. **72**, 980 (1984); **74**, 1033 (1985).

[35] K. Ikeda, Opt. Commun. **30**, 257 (1979).

[36] Ch. Häger and F. Kaiser, Appl. Phys. B **55**, 132 (1992).

[37] M. C. Mackey and L. Glass, Science **197**, 287 (1977).

[38] J. Mallet-Paret, J. Diff. Eq. **22**, 331 (1976).

[39] M. Le Berre, E. Ressayre, A. Tallet, H. M. Gibbs, D. L. Kaplan, and M. H. Rose, Phys. Rev. A **35**, 4020 (1987).

[40] J. D. Farmer, Physica D **4**, 366 (1982).

[41] K. Ikeda and K. Matsumoto, J. Stat. Phys. **44**, 955 (1986).

[42] S. Lepri, G. Giacomelli, A. Politi, and F. T. Arecchi, Physica D **70**, 235 (1993).

[43] L. Flepp, Ph.D. thesis, Zürich University, 1991 (unpublished).

[44] J. Simonet, M. Warden, and E. Brun, Phys. Rev. E **50**, 3383 (1994).

[45] A. Abragam, *Principles of Nuclear Magnetism* (Oxford University Press, Oxford, 1989).

[46] K. Ikeda, K. Kondo, and O. Akimoto, Phys. Rev. Lett. **49**, 1467 (1982).

[47] G. Broggi, J. Opt. Soc. Am. B **5**, 1020 (1988).

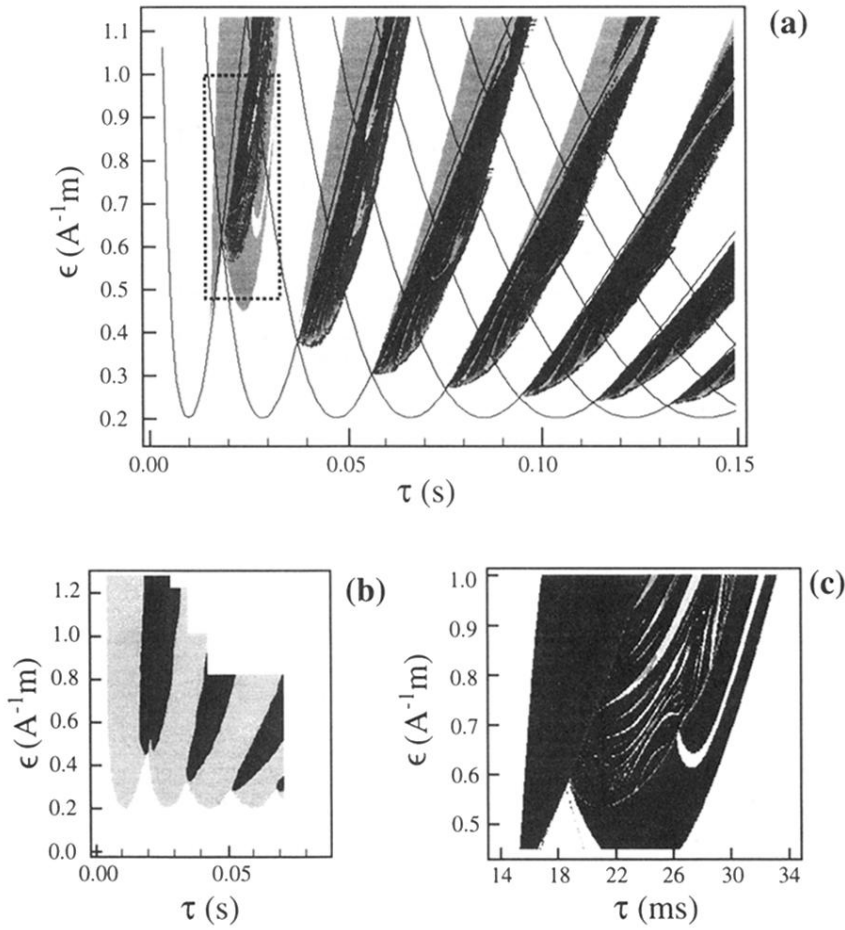[48] G. Giacomelli, R. Meucci, A. Politi, and F. T. Arecchi, Phys. Rev. Lett. **73**, 1099 (1994).

FIG. 3. Overview of the phenomenology in parameter space (τ, ϵ). The gray coding corresponds to the number of different maxima detected in a fixed finite portion of the signal. The white region corresponds to the stable fixed points, light gray to a stable limit cycle, and darker regions to signals with increasing number of different maxima (including chaotic behavior): (a) model, (b) experiment, and (c) enlargement of the boxed area in (a).